JOURNAL OF SPACECRAFT AND ROCKETS
Vol. 38, No. 5, September–October 2001

X-33 Aerodynamic Computations and Comparisons with Wind-Tunnel Data

Brian R. Hollis,* Richard A. Thompson,† Kelly J. Murphy,† Robert J. Nowak,*
Christopher J. Riley,‡ William A. Wood,† and Stephen J. Alter‡
NASA Langley Research Center, Hampton, Virginia 23681
and
Ramadas K. Prabhu§
Lockheed Martin Engineering and Sciences, Hampton, Virginia 23681

A computational fluid dynamics study conducted at the NASA Langley Research Center to support the phase II development of the X-33 vehicle is detailed. Aerodynamic computations for the X-33 vehicle were performed using two finite volume, Navier–Stokes solvers and an inviscid Euler code. Computations were made for a range of wind-tunnel test conditions from Mach 4.63 to 10.0 with angles of attack from 10 to 48 deg and body flap deflections of 0, +10, and +20 deg. Additional computations were performed over a parametric range of freestream conditions with Mach numbers of 4–10 and angles of attack of 10–50 deg. Computational results and comparisons with wind-tunnel aerodynamic data are presented.

Nomenclature

a	=	speed of sound, m/s
b	=	wing span, m
C_A	=	axial force coefficient
C_m	=	pitching moment coefficient
C_N	=	normal force coefficient
L	=	length, m
L/D	=	lift-to-drag ratio
M	=	Mach number
Re	=	Reynolds number, 1/m
S	=	reference area, m^2
T	=	temperature, K
U	=	velocity, m/s
α	=	angle of attack, deg
δ_{BF}	=	body flap deflection, deg
Δs	=	wall cell height, m
μ	=	viscosity, kg/(m · s)
ρ	=	density, kg/m^3

Introduction

THE X-33 vehicle will be a subscale technology demonstrator for an economical, full-scale, single-stage-to-orbit reusable launch vehicle (SSTO-RLV). It is intended to prove the feasibility of the SSTO-RLV concept through demonstration of key design and operational aspects of the vehicle. Additional background on the X-33 program is provided in Refs. 1–5.

As part of an industry/government partnership in the X-33 program, the NASA Langley Research Center (LaRC) was tasked to provide aerodynamic and aeroheating results to support the design and development of the vehicle. Earlier results of this work have been presented by Hamilton et al.,[6] and Thompson et al.[7] The current research program is detailed in companion papers by Berry et al.,[8] Hollis et al.,[9] Horvath et al.,[10] Murphy et al.,[11] and Thompson.[12] In this paper, aerodynamic performance predictions from two Navier–Stokes codes and an inviscid Euler code are presented and compared with data from several supersonic and hypersonic wind tunnels. Aerodynamic computations for a parametric range of Mach numbers and angles of attack are also presented.

Received 23 July 2000; revision received 7 November 2000; accepted for publication 5 February 2001.

*Aerospace Technologist, Aerothermodynamics Branch, Aerodynamics, Aerothermodynamics, and Acoustics Competency. Member AIAA.
†Aerospace Technologist, Aerothermodynamics Branch, Aerodynamics, Aerothermodynamics, and Acoustics Competency.
‡Aerospace Technologist, Aerothermodynamics Branch, Aerodynamics, Aerothermodynamics, and Acoustics Competency. Senior Member AIAA.
§Senior Aerospace Engineer.

X-33 Geometry

A brief history of the X-33 configuration evolution through phase II of the program is presented in Ref. 10. The current configuration (Fig. 1) is a lifting-body delta planform with twin vertical tails, canted fins, and body flaps. The body length is 19.3 m (63.2 ft) from the nose to the end of the engine module, and the span across the canted fins is 23.2 m (76.1 ft). The canted fins have a dihedral of 20 deg and a −8.58-deg incidence angle. Reference dimensions for aerodynamic coefficients are given in Table 1.

Computational results presented in this paper are based on the F-Loft, Rev-F configuration (Lockheed designation 604B002F) and experimental results are based on the F-Loft, Rev-G configuration (Lockheed designation 604B002G). The overall given dimensions apply to both configurations, which differ only in that the Rev-G configuration has minor modifications to the aft, upper surface of the vehicle, which should have no impact on the high-angle-of-attack hypersonic cases discussed in this paper.

Computational Methods

Numerical Algorithms

Computational predictions for comparisons with wind tunnel test data were generated using the Navier–Stokes solvers GASP[13] and LAURA[14,15] and the inviscid solver FELISA.[16,17] Wind-tunnel computations were performed with GASP and LAURA using a laminar, perfect-gas thermochemical model and with FELISA using an inviscid, perfect-gas model. Additional wind-tunnel cases were computed with a CF_4 thermochemical model using LAURA and FELISA. Perfect-gas cases were also computed across a parametric M–α range using GASP.

The GASP code[13] is a three-dimensional, finite volume, Navier–Stokes solver that incorporates numerous flux formulations, total variation diminishing limiters, thermochemical models, turbulence models, and time-integration methods. As discussed in Ref. 9, a third-order, upwind-biased, min–mod limited scheme, with a Roe[18] flux formulation in the body-normal direction and a Van Leer[19] formulation in the other two directions, was identified as the best set of options for generating accurate predictions. Full viscous terms were retained for all three directions. The Jacobi scheme was used for time integration. The perfect-gas model was used for all cases.

The LAURA code[14,15] is a three-dimensional Navier–Stokes solver based on a point-implicit relaxation scheme and Roe[18] averaging with Yee's[20] symmetric total variation diminishing limiter for inviscid fluxes. The code includes perfect-gas, equilibrium, and nonequilibrium air models and a CF_4 thermochemical model. The perfect-gas air and CF_4 models were used for the wind-tunnel cases.

The FELISA[16,17] software package consists of a set of codes used for the generation of unstructured, three-dimensional, tetrahedral grids and the solution of the steady, three-dimensional Euler equations on those grids. FELISA includes solvers for both transonic and hypersonic flows and thermochemical models for air (perfect-gas and equilibrium) and CF_4. For the cases discussed in this paper, the hypersonic solver was used with the perfect-gas air and CF_4 thermochemical models. The FELISA volume grid generation software is discussed in Ref. 16, and the hypersonic solver is discussed in Ref. 17. Further details of the FELISA X-33 computations are presented in Ref. 21.

Grid Generation and Adaption

The GASP and LAURA Navier–Stokes flowfield computations were performed on a single-block, half-body, structured grid[22] (Fig. 2). Grid scale was 0.7% to match the wind-tunnel test model. To lessen the computational requirements, the engine module and wake were not included in this grid, and a fake-wake, solid-body representation was employed for the regions between the canted fins and the ends of the body flaps as well as between the body flaps. Note that this fake-wake surface was not included when integrating surface pressure loads to determine aerodynamic coefficients. The baseline grid, which was used for all LAURA computations, had $(254 \times 181 \times 65)$ points in the longitudinal, circumferential, and

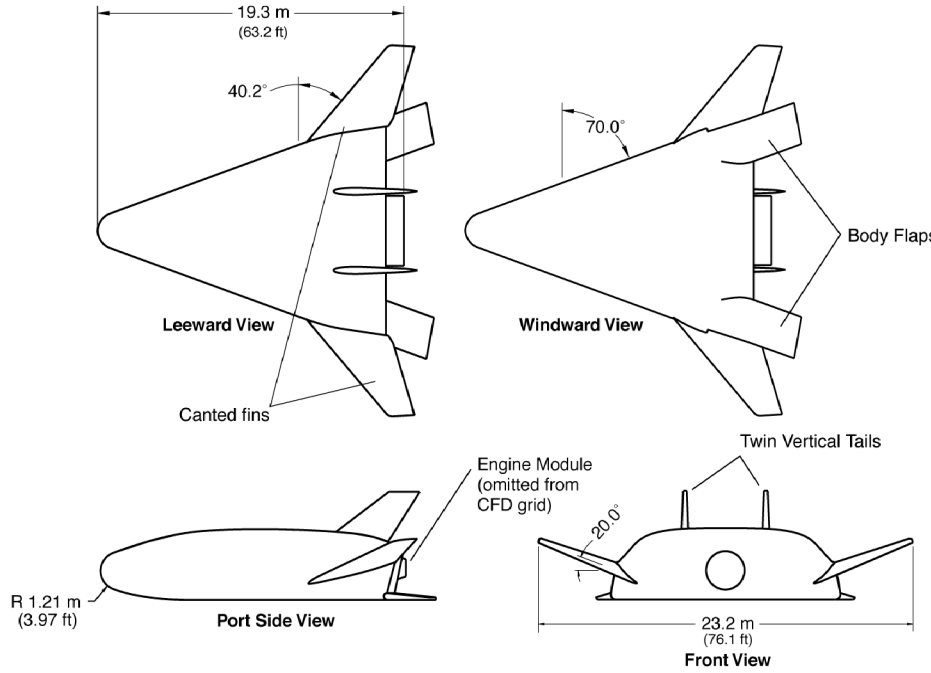

Fig. 1 Full-scale X-33 F-Loft, Rev-F vehicle.

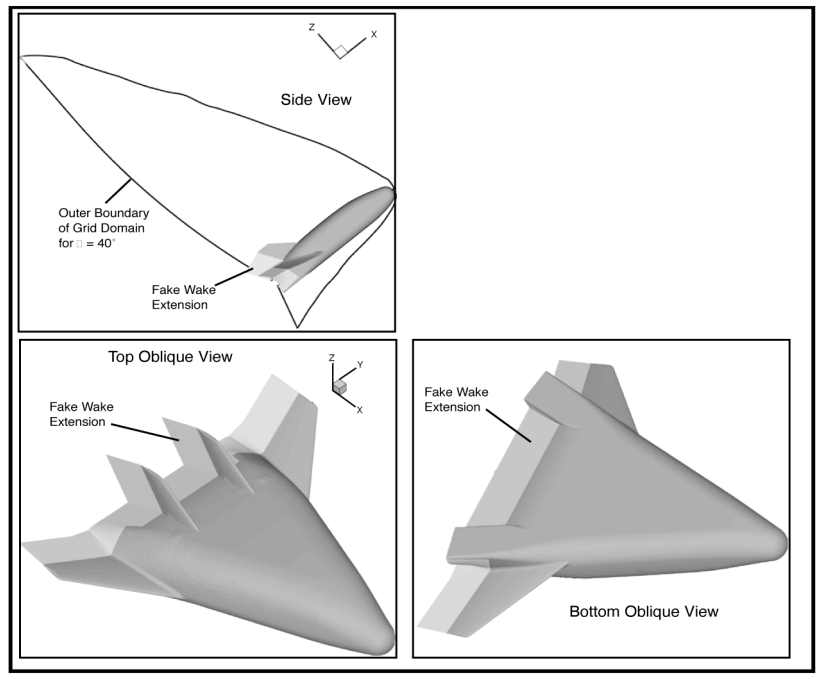

Fig. 2 X-33 computational surface geometry with fake-wake extension.

normal directions, respectively. The number of grid points was decreased for the GASP computations to ($127 \times 181 \times 65$). The lower density of the GASP grid was shown to be sufficient for aeroheating computations in Ref. 9 and so should also be sufficient for aerodynamic computations. Additionally, a series of parametric M–α computations was performed with GASP on a ($65 \times 91 \times 33$) point grid to investigate aerodynamic trends. A single GASP computation was also performed on a full-wake grid, which included the engine module to determine if the fake-wake approximation had any significant effects on the computed aerodynamic parameters. This full-wake grid had 15 blocks with a total of 2.7×10^6 grid points.

For each angle-of-attack case, grid adaption was performed to align the outer domain of the grid with the bow shock and to cluster grid points within the wall boundary layer. Typically, the outer boundary was adjusted so that the shock was located at approximately 80% of the normal distance between the wall and outer grid boundary. Approximately 50% of the normal grid points were clustered within the wall boundary layer, and the wall cell Reynolds number ($Re_w = \rho a \Delta s / \mu_w$) was set in the range of 10–20. The scheme employed to perform these manipulations is based on that described in Ref. 15. When necessary, additional grid quality refinement and smoothing were performed using the Volume Grid Manipulation code.[23]

The FELISA inviscid computations were performed on unstructured tetrahedral volume grids generated with the FELISA software package. Because the inviscid code is not capable of simulating separated flow regions, the wake of the vehicle was not included in the grid, and a fake-wake extension was employed as was done with the structured grid. Separate grids were generated for each of the different sets of FELISA wind-tunnel computations. The number of tetrahedrons in the grids varied from 6.5×10^6 to 7.9×10^6.

Experiment Background

The experimental aerodynamic tests that complement this study are presented in detail in Ref. 11. The goal of these tests was to define the aerodynamic performance of the X-33 vehicle. The aerodynamic data reported in Ref. 11 were acquired in the LaRC 20-Inch Mach 6 Air Tunnel, 31-Inch Mach 10 Air Tunnel, 20-Inch Mach 6 CF_4 Tunnel, and Unitary Plan Wind Tunnel (UPWT). Information on the first three facilities can be found in Ref. 24, and the UPWT is described in Ref. 25.

Aerodynamic testing of the F-Loft, Rev-G (604B0002G) configuration was conducted with a 0.7%-scale metallic force-and-moment model. Data were obtained for angles of attack from −4 to +48 deg with body flap deflections from −15 to +30 deg. Test Mach numbers in the various facilities ranged from 4.63 to 10, with Reynolds numbers from 1.6×10^5/m to 2.5×10^7/m (0.05×10^6/ft to 7.5×10^6/ft). A complete discussion of test parametrics is presented in Ref. 11. A limited uncertainty analysis is presented in that reference, in which an uncertainty corresponding to ±0.5% of the full-scale range of the force-and-moment balance is applied to all aerodynamic data.

Table 1 Reference dimensions for X-33 F-Loft, Rev-F

Dimension	Full scale	0.7%
S_{ref}	149.4 m^2 (1608 ft^2)	0.732 cm^2
L_{ref}, L	19.3 m (63.2 ft)	13.5 cm
B	23.2 m (76.1 ft)	16.2 cm
B_{ref}	11.2 m (36.6 ft)	7.84 cm
c.g.$_{ref}$	12.7 m (41.7 ft)	8.89 cm
R_{ref}	1.21 m (3.97 ft)	0.847 cm

Computational Results and Comparisons with Experimental Data

Results from the computations for wind-tunnel conditions are presented in this section and compared with experimental data. Results from the M–α parametric computations are also presented. Computed and measured aerodynamic performance is discussed in terms of the normal force C_N and axial force coefficients C_A, lift C_L and drag coefficients C_D, and the pitching moment coefficient C_m.

Freestream and Boundary Conditions

Wind-tunnel test case computations were performed for the operating conditions of the NASA Langley 20-Inch Mach 6 Air Tunnel, 31-Inch Mach 10 Air Tunnel, 20-Inch Mach 6 CF_4 Tunnel, and UPWT, and additional cases were computed in a M–α parametric space bounded by Mach numbers of 4.0 and 10.0 and angles of attack of 10 and 50 deg. Freestream conditions for all of these cases are listed in Table 2. The wall boundary condition was set to a uniform temperature of 300 K.

Aerodynamics for M–α Parametric Space Cases

To investigate the effects of Mach number and angle of attack on the aerodynamics of the X-33 vehicle, a series of perfect-gas GASP computations was performed across a range of Mach numbers from 4.0 to 10.0 and angles of attack from 10 to 50 deg with 0-deg body flap deflections. A constant Reynolds number of 6.59×10^6/m (2.01×10^6/ft) was maintained for all computations. The freestream temperatures for the cases were determined by linear interpolation as a function of Mach number with the temperatures anchored to the nominal operating conditions of the Mach 6 Air and Mach 10 Air wind tunnels.

Results from these computations are presented in Figs. 3–8. The predictions for the force coefficients, C_A, C_N, C_L, and C_D, and the lift-to-drag ratio L/D all show similar behavior, with the coefficient vs angle-of-attack curves for each variable decreasing as Mach number increases (Figs. 3–4 and 6–8). A trend toward Mach number independence can also be identified by noting that the differences between the curves decrease with increasing Mach number.

Table 3 Differences in coarse and fine grid aerodynamic predictions for Mach 10 cases

	GASP		
Coefficient	$127 \times 181 \times 65$	$65 \times 91 \times 33$	% Difference
C_A at $\alpha = 20$	0.1202	0.1206	+0.33
C_N at $\alpha = 20$	0.3391	0.3388	−0.09
C_m at $\alpha = 20$	0.0113	0.0114	+0.88
C_A at $\alpha = 30$	0.1192	0.1195	+0.25
C_N at $\alpha = 30$	0.6833	0.6813	−0.30
C_m at $\alpha = 30$	0.0071	0.0073	+2.82
C_A at $\alpha = 40$	0.1143	0.1144	+0.09
C_N at $\alpha = 40$	1.0541	1.0544	+0.03
C_m at $\alpha = 40$	0.0022	0.0019	−13.6

Table 2 Flow conditions for wind-tunnel cases

Case	Mach	T_∞, K	ρ_∞, kg/m^3	U_∞, m/s	Re_∞, 1/m	α, deg
20-Inch Mach 6 Air	5.99	62.1	6.28e−2	945.1	1.33e7	12, 20, 24, 30, 36, 40, 48
31-Inch Mach 10 Air	9.98	48.9	1.71e−2	1414.0	6.84e6	12, 20, 24, 30, 36, 40, 48
Unitary Plan Wind Tunnel	4.63	65.0	7.45e−2	742.2	1.18e7	24, 36, 48
20-Inch Mach 6 CF_4	6.02	170	1.77e−2	849.3	1.48e6	24, 36, 48
M–α parametrics	4.0	68.0	4.88e−2	660.1	6.59e6	10, 20, 30, 40
	5.0	65.0	3.81e−2	807.6	6.59e6	10, 20, 30, 40, 50
	6.0	62.0	3.10e−2	946.4	6.59e6	10, 20, 30, 40, 50
	8.0	56.0	2.20e−2	1198.4	6.59e6	10, 20, 30, 40, 50
	10.0	50.0	1.66e−2	1413.8	6.59e6	10, 20, 30, 40, 50

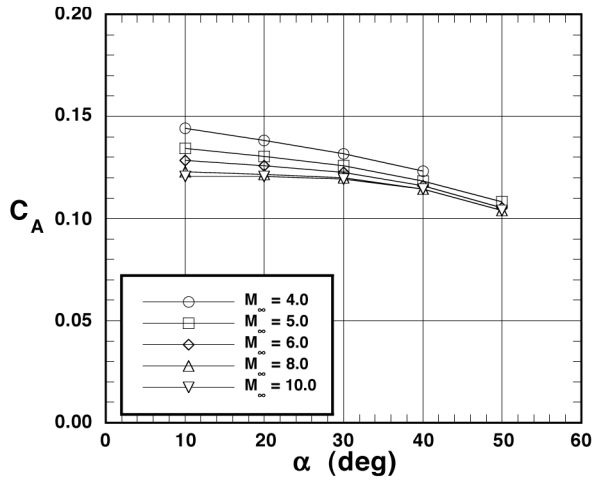

Fig. 3 GASP computations for variation of axial force coefficient with Mach number and angle of attack.

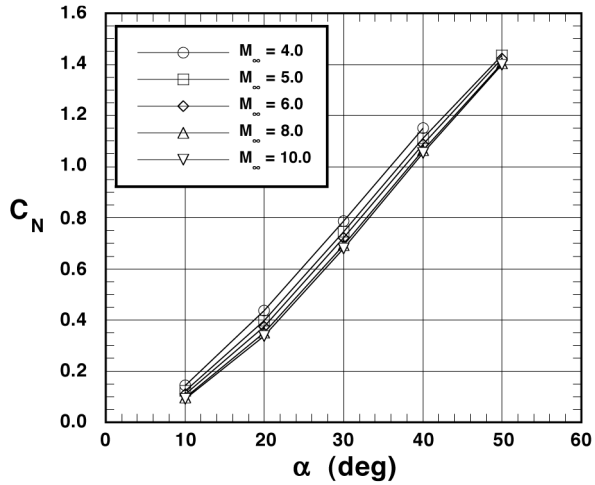

Fig. 4 GASP computations for variation of normal force coefficient with Mach number and angle of attack.

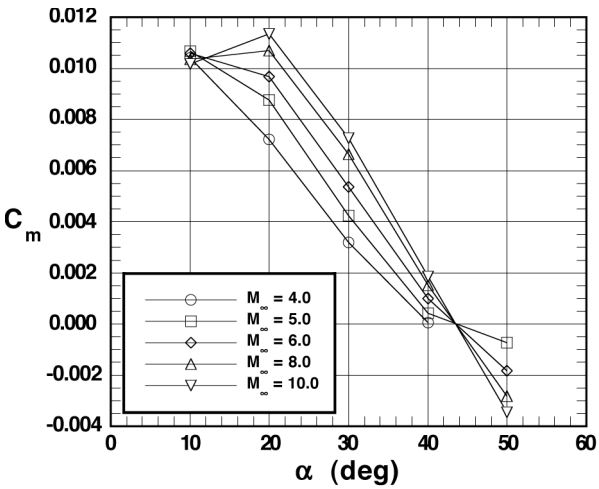

Fig. 5 GASP computations for variation of pitching moment coefficient with Mach number and angle of attack.

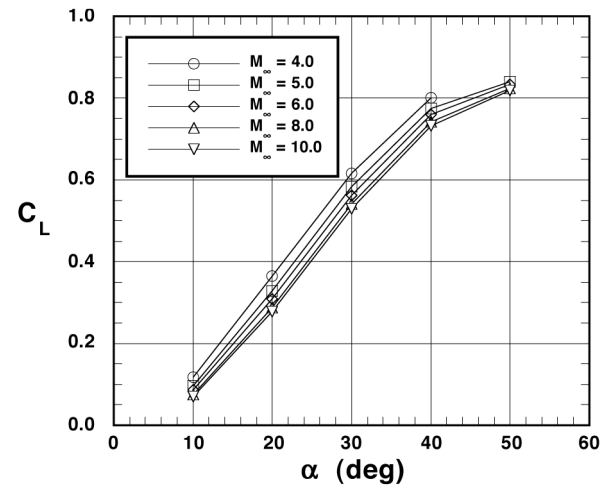

Fig. 6 GASP computations for variation of lift coefficient with Mach number and angle of attack.

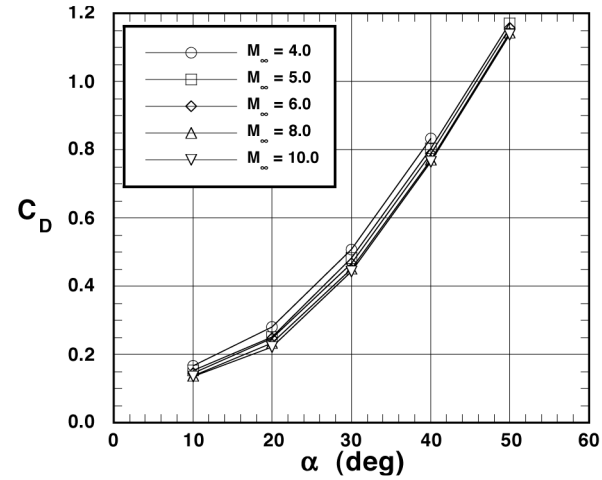

Fig. 7 GASP computations for variation of drag coefficient with Mach number and angle of attack.

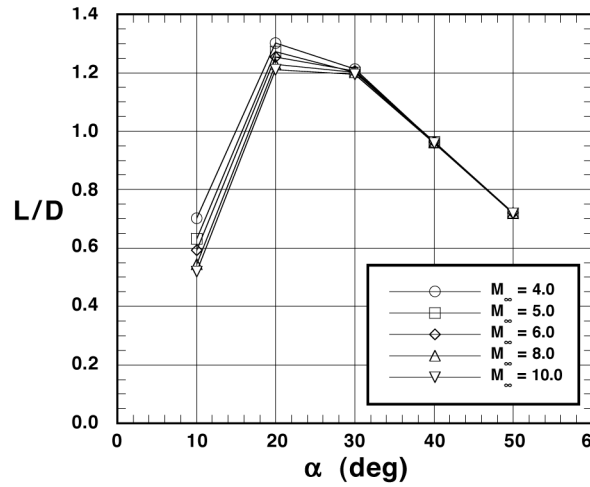

Fig. 8 GASP computations for variation of lift-to-drag ratio with Mach number and angle of attack.

However, the pitching moment coefficient behavior differs from that of the other coefficients in that a stronger Mach number dependency is observed (Fig. 5). For angles of attack above 20 deg, a consistent trend can be observed of a stable pitching moment curve ($\partial C_m/\partial\alpha < 0$) with the magnitude of C_m increasing with increasing Mach number. The trim point ($C_m = 0$) appears to be nearly Mach independent at around 43 deg. Also, the C_m curves all appear to be tending toward instability somewhere below $\alpha = 20$ deg, depending on Mach number.

These M–α parametric space computations were performed on a coarser grid ($65 \times 91 \times 33$) than the other GASP computations with the intent of identifying trends rather than producing quantitative results. However, as shown in Table 3 by comparisons of aerodynamic coefficients on this coarse grid with GASP computations on the finer grid ($127 \times 181 \times 65$) for the 31-Inch Mach 10 Air Tunnel cases, the accuracy of these coarser grid results is almost as good as the those on the finer grid, at least for aerodynamics. The parametric computations are within less than $\pm 1\%$ of the finer grid

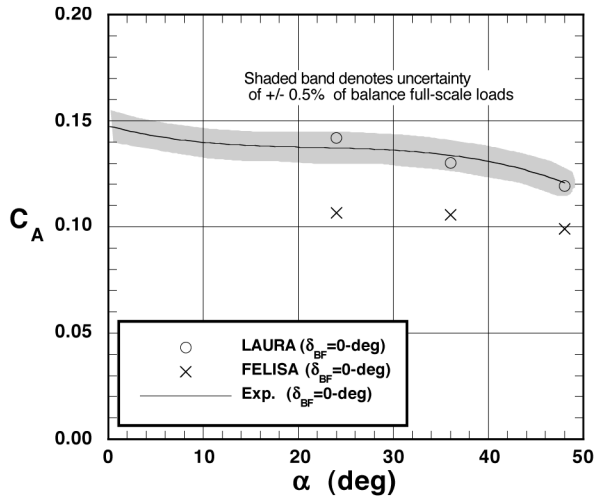

Fig. 9 Comparison of measured and predicted axial force coefficient for 20-Inch Mach 6 CF_4 tunnel.

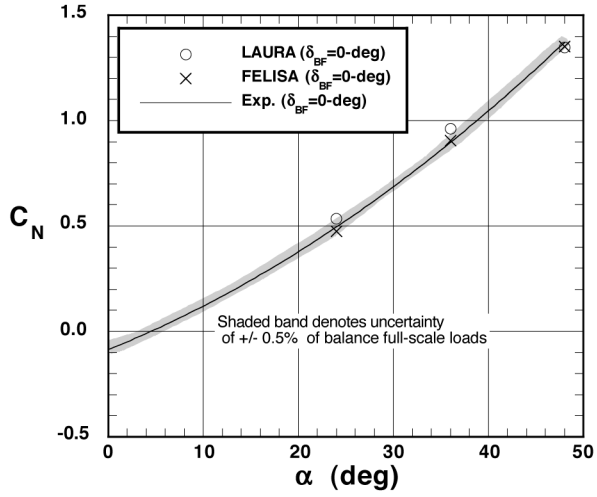

Fig. 10 Comparison of measured and predicted normal force coefficient for 20-Inch Mach 6 CF_4 tunnel.

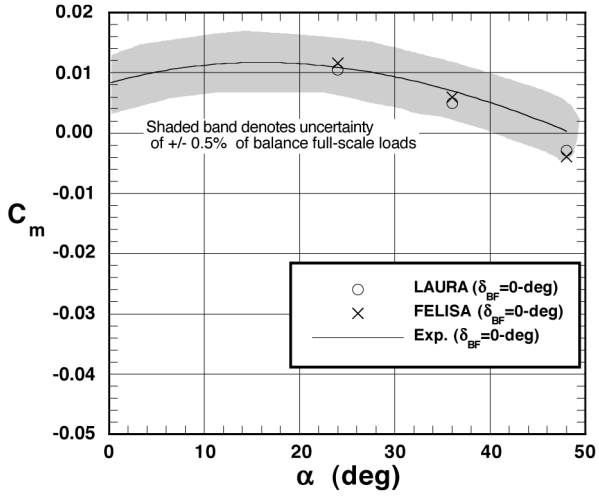

Fig. 11 Comparison of measured and predicted pitching coefficient for 20-Inch Mach 6 CF_4 tunnel.

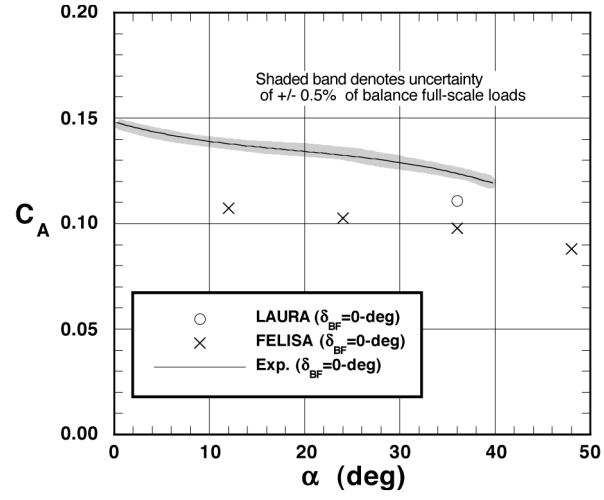

Fig. 12 Comparison of measured and predicted axial force coefficient for UPWT.

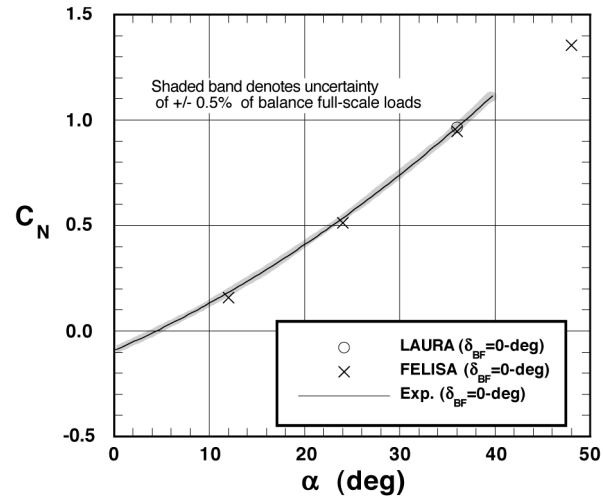

Fig. 13 Comparison of measured and predicted normal force coefficient for UPWT.

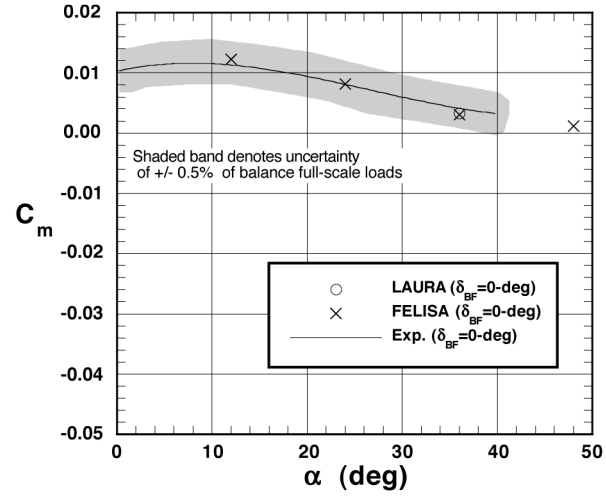

Fig. 14 Comparison of measured and predicted pitching moment coefficient for UPWT.

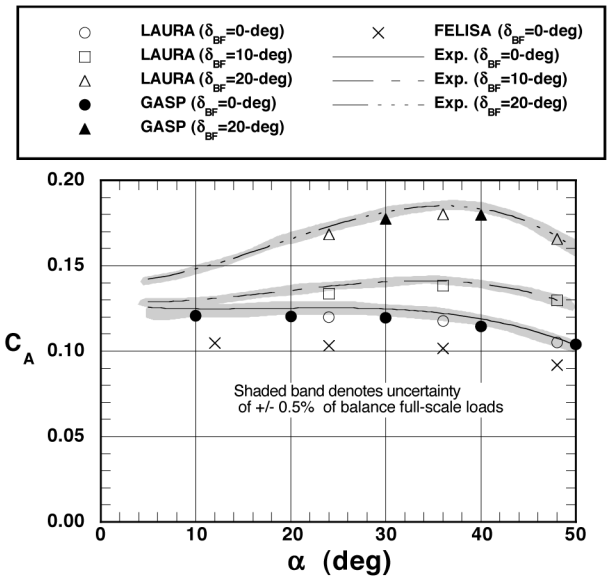

Fig. 15 Comparison of measured and predicted axial force coefficient for 31-Inch Mach 10 Air Tunnel.

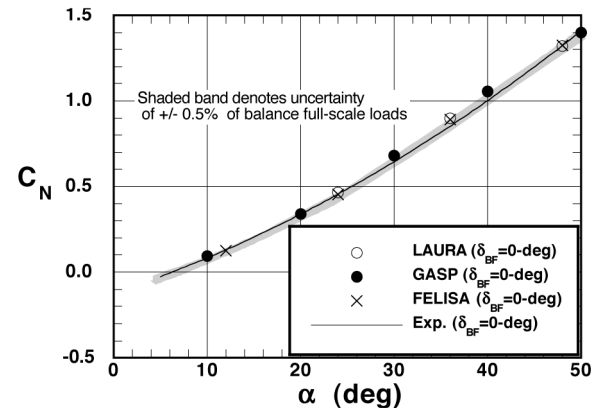

Fig. 16 Comparison of measured and predicted normal force coefficient for 31-Inch Mach 10 Air Tunnel.

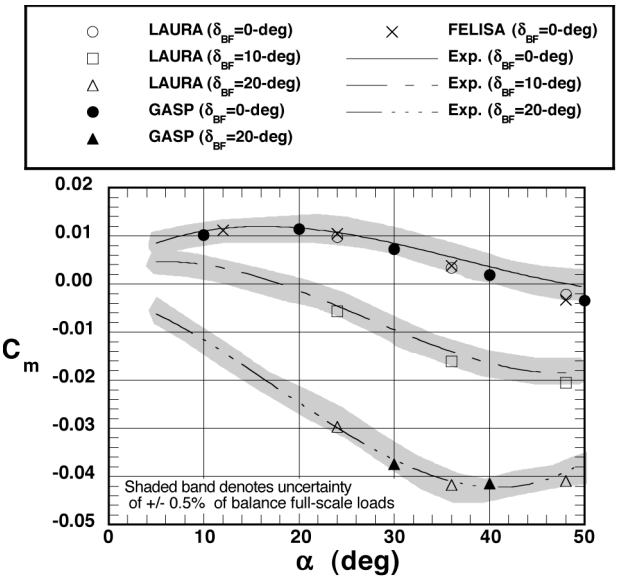

Fig. 17 Comparison of measured and predicted pitching moment coefficient for 31-Inch Mach 10 Air Tunnel.

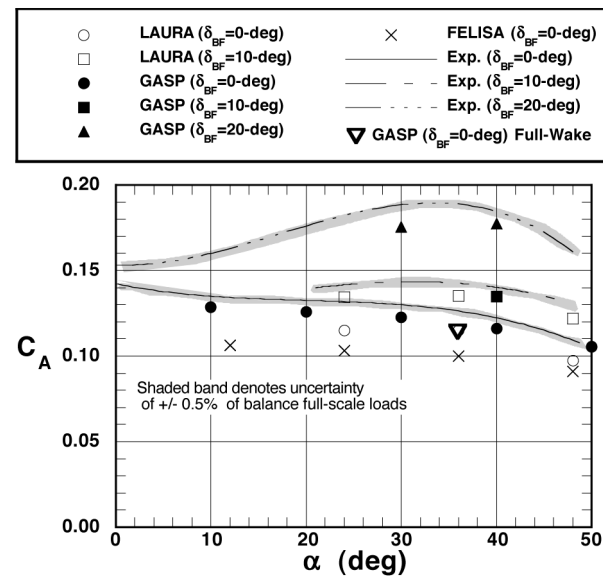

Fig. 18 Comparison of measured and predicted axial force coefficient for 20-Inch Mach 6 Air Tunnel.

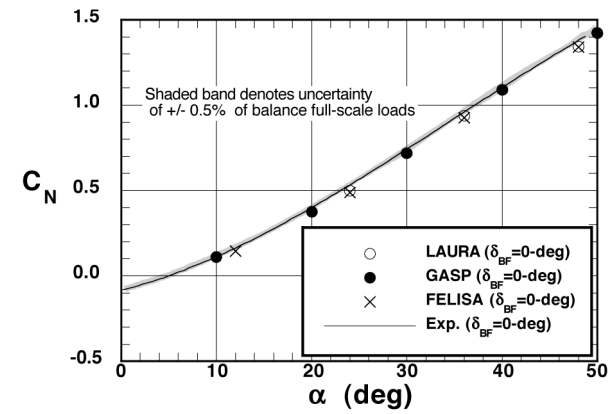

Fig. 19 Comparison of measured and predicted normal force coefficient for 20-Inch Mach 6 Air Tunnel.

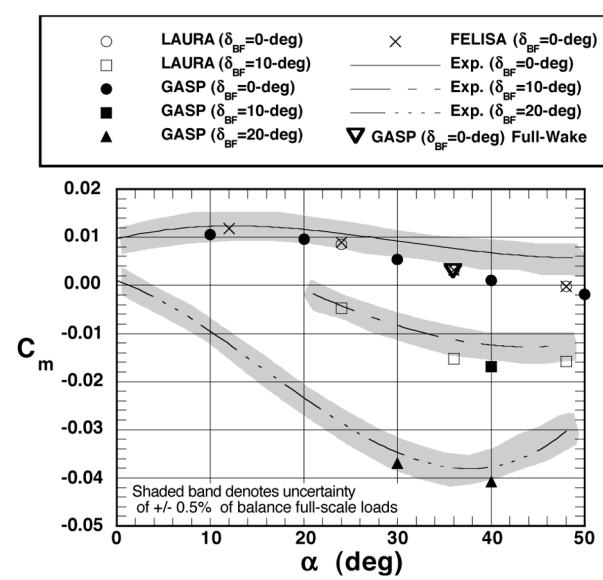

Fig. 20 Comparison of measured and predicted pitching moment coefficient for 20-Inch Mach 6 Air Tunnel.

computations except for the pitching moment at $\alpha = 30$ and 40 deg, where the value of this coefficient is approaching zero.

Aerodynamics for Wind-Tunnel Cases

Aerodynamic predictions for each of the wind-tunnel cases are presented in this section. Normal force, axial force, and pitching moment coefficients are plotted vs angle of attack for each case, and curve fits to the experimental data from Ref. 11 are shown. Uncertainty bounds on each coefficient resulting from the $\pm 0.5\%$ of the balance full-scale-load uncertainty estimate are also indicated on each plot by a shaded band outlining the curve fit. Where available, C_A and C_m predictions and data for body flap deflections of +10 and +20 deg are presented in addition to the 0-deg body flap cases. Body flap deflections had little effect on the normal force, and so only 0-deg body flap values are shown for C_N.

LAURA and FELISA aerodynamic predictions for the 20-Inch Mach 6 CF_4 cases are presented in Figs. 9–11. Results from both codes are in close agreement with the normal force and pitching moment coefficient data. LAURA results are in close agreement with the axial force data. Because the axial forces due to viscous effects are not accounted for in the inviscid FELISA computations, these predictions are significantly lower than the data.

LAURA and FELISA results for the UPWT cases are shown in Figs. 12–14. For C_N and C_m, both codes again agree with the data to within the experimental uncertainty. The inviscid FELISA C_A values are again, as expected, lower than the data, whereas the LAURA prediction is slightly outside of the lower uncertainty bound.

GASP, LAURA, and FELISA computations for the 31-Inch Mach 10 Air Tunnel cases and 20-Inch Mach 6 Air Tunnel cases are shown in Figs. 15–17 and 18–20, respectively. Note that results for +10- and +20-deg deflected body flaps cases are also included in these plots. The inflections in the +10- and +20-deg flap deflection pitching moment curves for both tunnels at high angles of attack were found to result from a bow-shock/flap-shock interaction. This interaction is discussed in more detail in the subsequent "Bow-Shock/Flap-Shock Interaction" section.

For the Mach 10 cases, the GASP, LAURA, and FELISA predictions for all variables are within the experimental uncertainty except for the FELISA C_A predictions. For the Mach 6 cases, normal force computations are within the experimental uncertainty, but both axial force and pitching moment computations underpredict the data. These differences between computation and experiment are relatively constant for C_A, but increase with angle of attack for C_m.

The reason for the differences in the Mach 6 results has not been determined, but the effects of excluding the wake from the computations were examined by running a full-wake computation. As shown in Fig. 20, the pitching moment coefficient from a GASP 15-block, full-wake computation for the Mach 6, $\alpha = 36$ deg case differs only slightly from that of the LAURA fake-wake computation for the same point. This agreement would suggest that the fake-wake representation is not the cause of the pitching moment discrepancies.

As discussed by Murphy et al.,[11] the pitching moment differences will not significantly affect the stability and control performance of the X-33. At high angles of attack, this difference is of the same magnitude as the pitching moment change produced by only a few degrees of body flap deflection. The X-33 vehicle is designed with a +30-deg body flap deflection range, but in hypersonic, high angle-of-attack flight, the vehicle is close to being trimmed without any body flap deflections. Thus, considerable excess control ability is available to account for any uncertainties in the pitching moment predictions or experimental data.

Bow-Shock/Flap-Shock Interaction

Computations for the 31-Inch Mach 10 Air Tunnel and 20-Inch Mach 6 Air Tunnel cases revealed the existence of an interaction at high angles of attack between the bow shock and the shocks created by the flaps when they are deflected to +10 or +20 deg. This interaction can also be seen in the heating data presented in Ref. 10. The wave system created by this interaction is illustrated by the pressure contours plotted in Fig. 21. Note that the shock interaction produces an expansion fan, which impinges on the trailing edge of the flap. The lower pressure behind this expansion wave decreases the efficiency of the flaps, which causes the pitching moment to begin increasing at higher angles of attack. This effect can be seen in the +10- and +20-deg flap deflection pitching moments plotted in Figs. 17 and 20. This interaction also affects the flap heating environment, as discussed in Ref. 9.

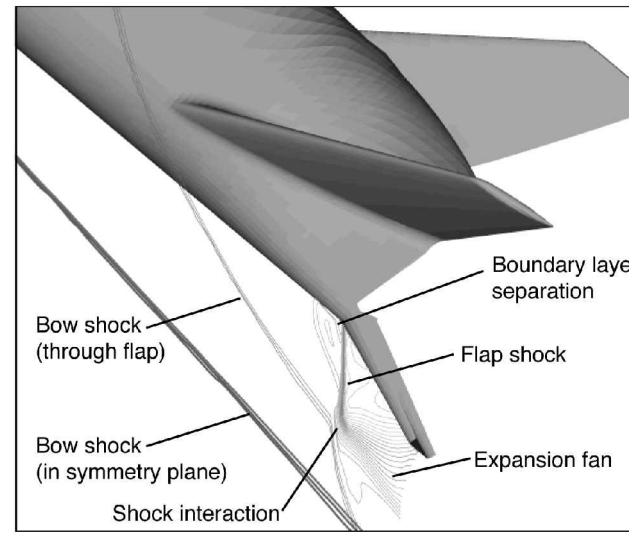

Fig. 21 Pressure contours showing shock–shock interaction for Mach 6, α = 40 deg case.

Summary

Computations have been performed using the GASP and LAURA Navier–Stokes codes and the FELISA inviscid Euler code to predict the aerodynamic characteristics of the X-33 phase II vehicle. These predictions were compared with wind-tunnel aerodynamic data obtained in supersonic and hypersonic wind tunnels.

Aerodynamic computations for each of the four wind tunnels were found to fall within the estimated experimental uncertainty of the data except for the FELISA axial force predictions and some of the axial force and pitching moment predictions (from all codes) at the higher angles of attack for the 20-Inch Mach 6 Air Tunnel cases. The FELISA axial force discrepancies were expected and were due to the absence of viscous axial force contributions in an inviscid solver. The pitching moment discrepancies were not resolved but were relatively small and well within the control authority of the X-33 vehicle.

The close agreement between computational and experimental results presented in this paper complements the experimental aerodynamic database used in the design of the X-33 vehicle and the optimization of its trajectories by providing a greater measure of confidence to the experimental results. Furthermore, the computations added points to the database that were not covered in the wind-tunnel tests. The computations also showed that an interaction between the bow and body flap shocks was the cause of the degradation of the pitching moment contribution of the body flaps at high angles of attack.

References

[1]Bekey, I., Powell, R., and Austin, R., "NASA Studies Access to Space," *Aerospace America*, Vol. 32, No. 5, 1994, pp. 38–43.

[2]Cook, S. A., "X-33 Reusable Launch Vehicle Structural Technologies," AIAA Paper 96-4563, Nov. 1996.

[3]Freeman, D. C., Jr., Talay, T. A., and Austin, R. E., "Reusable Launch Vehicle Technology Program," International Astronautical Federation, Paper IAF 96-V.4.01, Oct., 1996.

[4]Powell, R. W., Lockwood, M. K., and Cook, S. A., "The Road from the NASA Access-to-Space Study to a Reusable Launch Vehicle," International Astronautical Federation, Paper IAF-98-V.4.02, Sept. 1998.

[5]Baumgartner, R. I., and Elvin, J. D., "Lifting Body–An Innovative RLV Concept," AIAA Paper 95-3531, Sept. 1995.

[6]Hamilton, H. H., II, Weilmuenster, K. J., Berry, S. A., and Horvath, T. J., "Computational/ Experimental Aeroheating Predictions for X-33 Phase II Vehicle," AIAA Paper 98-0869, Jan. 1998.

[7]Thompson, R. A., Hamilton, H. H., II, Berry, S. A., and Horvath, T. J., "Hypersonic Boundary Layer Transition for X-33 Phase II Vehicle," AIAA Paper 98-0867, Jan. 1998.

[8]Berry, S. A., Horvath, T. J., Hollis, B. R., Thompson, R. A., and Hamilton, H. H., II, "X-33 Hypersonic Boundary-Layer Transition," *Journal of Spacecraft and Rockets*, Vol. 38, No. 5, 2001, pp. 646–657.

[9]Hollis, B. R., Horvath, T. J., Berry, S. A., Hamilton, H. H., II, Thompson, R. A., and Alter, S. J., "X-33 Computational Aeroheating Predictions and Comparisons with Experimental Data," *Journal of Spacecraft and Rockets*, Vol. 38, No. 5, 2001, pp. 658–669.

[10]Horvath, T. J., Berry, S. A., Hollis, B. R., Liechty, D. S., Hamilton, H. H., II, and Merski, N. R., "X-33 Experimental Aeroheating at Mach 6 Using Phosphor Thermography," *Journal of Spacecraft and Rockets*, Vol. 38, No. 5, 2001, pp. 634–645.

[11]Murphy, K. J., Nowak, R. J., Thompson, R. A., Hollis, B. R., and Prabhu, R., "X-33 Hypersonic Aerodynamic Characteristics," *Journal of Spacecraft and Rockets*, Vol. 38, No. 5, 2001, pp. 670–683.

[12]Thompson, R. A., "Review of X-33 Hypersonic Aerodynamic and Aerothermodynamic Development," 22nd International Congress of the Aeronautical Sciences, Rept. ICA-0323, Aug.–Sept. 2000.

[13]"GASP Version 3, The General Aerodynamic Simulation Program, Computational Flow Analysis Software for the Scientist and Engineer, User's Manual," AeroSoft, Inc., Blacksburg, VA, May 1996.

[14]Gnoffo, P. A., "An Upwind-Biased, Point-Implicit Algorithm for Viscous, Compressible Perfect-Gas Flows," NASA TP 2953, Feb. 1990.

[15]Cheatwood, F. M., and Gnoffo, P. A., "User's Manual for the Langley Aerothermodynamic Upwind Relaxation Algorithm (LAURA)," NASA TM 4674, April 1996.

[16]Peiro, J., Peraire, J., and Morgan, K., "FELISA System Reference Manual and User's Guide," TR, Univ. College, Swansea, Wales, U.K., 1993.

[17]Bibb, K. L., Periare, J., and Riley, C. J., "Hypersonic Flow Computation on Unstructured Meshes," AIAA Paper 97-0625, Jan. 1997.

[18]Roe, P. L., "Approximate Riemann Solvers, Parameter Vectors and Difference Schemes," *Journal of Computational Physics*, Vol. 43, No. 2, 1981, pp. 357–372.

[19]Van Leer, B., "Flux Vector Splitting for the Euler Equations," *Proceedings of the 8th International Conference on Numerical Methods in Fluid Dynamics*, Springer-Verlag, Berlin, 1981.

[20]Yee, H. C., "On Symmetric and Upwind TVD Schemes," NASA TM 88325, 1990.

[21]Prabhu, R. K., "A Computational Study of an X-33 Configuration at Hypersonic Speeds," NASA/CR-1999-209366, July 1999.

[22]Alter, S. J., "Grid Generation Techniques Utilizing the Volume Grid Manipulator," AIAA Paper 98-3012, June 1998.

[23]Alter, S. J., "The Volume Grid Manipulator (VGM): A Grid Reusability Tool," NASA CR-4772, April 1997.

[24]Micol, J. R., "Hypersonic Aerodynamic/Aerothermodynamic Testing Capabilities at Langley Research Center: Aerothermodynamic Facilities Complex," AIAA Paper 95-2107, June 1995.

[25]Jackson, C. M., Corlett, W. A., and Monta, W. J., "Description and Calibration of the Langley Unitary Plan Wind Tunnel," NASA TP-1905, Sept. 1981.

T. C. Lin
Associate Editor